

# Two-dimensional hydrodynamic robust numerical model of soil erosion based on slopes and river basins

KANG Yongde<sup>1</sup>, HUANG Miansong<sup>2\*</sup>, HOU Jingming<sup>1\*</sup>, TONG Yu<sup>1</sup>, PAN Zhanpeng<sup>1</sup>

<sup>1</sup> State Key Laboratory of Eco-hydraulics in Northwest Arid Region of China, School of Water Resources and Hydroelectric Engineering, Xi'an University of Technology, Xi'an 710048, China;

<sup>2</sup> Beijing Capital Eco-Environment Protection Group Co. Ltd., Beijing 100028, China

**Abstract:** Erosion is an important issue in soil science and is related to many environmental problems, such as soil erosion and sediment transport. Establishing a simulation model suitable for soil erosion prediction is of great significance not only to accurately predict the process of soil separation by runoff, but also improve the physical model of soil erosion. In this study, we develop a graphic processing unit (GPU)-based numerical model that combines two-dimensional (2D) hydrodynamic and Green-Ampt (G-A) infiltration modelling to simulate soil erosion. A Godunov-type scheme on a uniform and structured square grid is then generated to solve the relevant shallow water equations (SWEs). The highlight of this study is the use of GPU-based acceleration technology to enable numerical models to simulate slope and watershed erosion in an efficient and high-resolution manner. The results show that the hydrodynamic model performs well in simulating soil erosion process. Soil erosion is studied by conducting calculation verification at the slope and basin scales. The first case involves simulating soil erosion process of a slope surface under indoor artificial rainfall conditions from 0 to 1000 s, and there is a good agreement between the simulated values and the measured values for the runoff velocity. The second case is a river basin experiment (Coquet River Basin) that involves watershed erosion. Simulations of the erosion depth change and erosion cumulative amount of the basin during a period of 1–40 h show an elevation difference of erosion at 0.5–3.0 m, especially during the period of 20–30 h. Nine cross sections in the basin are selected for simulation and the results reveal that the depth of erosion change value ranges from −0.86 to −2.79 m and the depth of deposition change value varies from 0.38 to 1.02 m. The findings indicate that the developed GPU-based hydrogeomorphological model can reproduce soil erosion processes. These results are valuable for rainfall runoff and soil erosion predictions on rilled hillslopes and river basins.

**Keywords:** soil erosion; two-dimensional modelling; rainfall runoff; Green-Ampt model; gully erosion

## 1 Introduction

Soil erosion is the foundation of soil and water conservation, watershed management, and nonpoint pollution control. It is also closely related to soil degradation, ecological restoration,

\*Corresponding author: HUANG Miansong (E-mail: hms@capitalwater.cn); HOU Jingming (E-mail: jingming.hou@xaut.edu.cn)

Received 2021-04-29; revised 2021-08-19; accepted 2021-08-27

© Xinjiang Institute of Ecology and Geography, Chinese Academy of Sciences, Science Press and Springer-Verlag GmbH Germany, part of Springer Nature 2021

dam construction, flood prediction, and water resources management. Soils need to be managed even as they respond to changes in rainfall. Storm rainfall is a key and dynamic factor in eroding soil, and most soil erosion is caused by rainstorm events. All of these factors have great impacts on both land use and soil erosion. Additionally, the potential impacts of climate change and water resources on the frequency and magnitude of rainfall in conjunction with subsequent changes in the form of land use are notable. Several studies have examined the relationship between rainfall response to erosion and the important factors that affect gully erosion change (Qin et al., 2018a, b). Individual heavy rainfall events can also cause severe soil erosion (Wang et al., 2016; Bryndal et al., 2017). Researchers have performed much work on the effects of individual rainfall events and rainfall intensity characteristics on soil erosion (Xu et al., 2013; Wang et al., 2016; Cerdà et al., 2017; dos Santos et al., 2017; Chen et al., 2018; Panagos and Katsoyiannis, 2019). Typically, severe soil erosion is caused by several heavy rainfall storms. The erosion process of the Loess Plateau in the arid region of Northwest China is very prominent, and some scholars have estimated the amount of erosion especially in the rill erosion process, which is very important to understand soil erosion in this area (e.g., Shen et al., 2016).

Rainfall plays an important role in soil erosion and transport because soil particles formed by erosion are transported to form gullies that hinder the further use of land (Woodward, 1999; Borrelli et al., 2017). Furthermore, more water flow energy is converted into kinetic energy for separation, which is entrained and transported, thereby exacerbating the erosion rate (Wirtz et al., 2010). Over the last decade, many indoor and outdoor experiments have been carried out to study soil erosion (González-Hidalgo et al., 2009; Taye et al., 2013; Wu et al., 2017, 2019; Qin et al., 2018a, b; Wang et al., 2018; Zhao et al., 2019; An et al., 2020). Empirical models are commonly used in field scale research of soil erosion, such as the Universal Soil Loss Equation (USLE) proposed by Wischmeier and Smith (1978) and the Revised Universal Soil Loss Equation (RUSLE) proposed by Renard et al. (1997). Most of these models are calculated using a series of measured data, and the changes in these data can explain soil erosion. The parameters in the empirical USLE and RUSLE models consider only the length and slope but ignore the spatial characteristics between rills and slope shape. In terms of the separate problem of gully erosion, scholars have aimed to model the rainfall erosion process through physical mechanisms (An and Liu, 2009; Qin et al., 2018a, b). The Water Erosion Prediction Project (WEPP) model was developed on the basis of actual physical processes; it defines erosion as the sum of material transport between rills. Similar physical models have also been developed and applied, such as the Kinematic Runoff and Erosion Model and European Soil Erosion Model (Smith et al., 1995; Morgan et al., 1998). In addition, there are other factors affecting the evolution processes of gully width, such as the discharge and slope (Bingner et al., 2016). Wells et al. (2013) found that with increases in the slope and flow rate between gullies, the width and widening rate of rills also gradually increased. The collapse process and physical mechanism of the sidewall for a slope caused by erosion are very complicated and are of widespread interest (Chaplot et al., 2011; Chen et al., 2013; Bingner et al., 2016). Although much research on soil erosion has been carried out and fruitful results have been achieved, the damage caused by gully erosion in different regions is still difficult to predict through existing models, and the parameters need to be localized. At present, numerical simulation techniques can simulate the above processes, but there are still some difficulties in quantitative simulation of erosion depth (Abderrezak et al., 2013; Wells et al., 2013; Bingner et al., 2016). Accordingly, further *in situ* experiments and model studies are needed to increase the understanding of ravine retreat (Chaplot et al., 2011). A better understanding of the gully expansion process is essential for the development of some water erosion prediction model modules (Wells et al., 2013; Bingner et al., 2016; de Lima et al., 2019) to protect erosive gullies.

Several researchers have developed two-dimensional (2D) runoff and soil erosion models that can simulate the spatial characteristics of rill erosion, which can determine the rainfall-runoff process and simulate the spatial characteristics of slope runoff (Govindaraju et al., 1992; Gottardi and Venutelli, 1993; Howes et al., 2006; Chen et al., 2013; Aksoy et al., 2016). However, these models lack physical modules that can characterize the process of soil erosion. Therefore,

one-dimensional (1D) and 2D coupled models were developed to simulate rainfall runoff and soil erosion processes on hillsides (Tayfur, 2007; An and Liu, 2009). Such models idealize the slope as a combination of some 1D aligned rills divided into 2D interrills. On this basis, 2D slope erosion models were established, but they cannot distinguish erosion between different rill configurations (Nord and Esteves, 2005). Although many results have been achieved in the past ten years, including 1D and 2D models, certain problems are not suitably solved; for example, there is a lack of information on distributed erosion that can reflect slope and trench erosion. Modelling methods may incorporate the quantitative prediction of soil erosion; however, the interaction mechanism of the spatial structure of rills and slope shape on rainfall and soil erosion processes is not clear.

The spatial characteristics of rills and nonplanar slopes of distributed models still lack research at the landscape scale. Some researchers have found that both rainfall and concave hillslopes dramatically affect soil erosion processes (Qin et al., 2018a, b; Tian et al., 2017; Batista et al., 2019). Furthermore, for both rill erosion and slope erosion, hillslopes can produce a series of depressions, which provide channels for surface runoff and sediment sources (Shen et al., 2016; Tian et al., 2017). The direction angle, local density, and spatial characteristics of width and depth of rills are crucial for runoff and soil erosion processes on slopes (Appels et al., 2011; Di Stefano et al., 2017, 2018; Wu et al., 2019). Slope shape is an important factor affecting slope flow and erosion (Sweeney et al., 2015). Different slope forms in nature may lead to various runoff and erosion characteristics, substantially, increasing the local rill shear stress and rill erosion (Gordon et al., 2012; Batista et al., 2019). Due to the complexity of slope erosion process (Stroosnijder, 2005), rainfall is unevenly distributed and complex, but sufficient representativeness plays a very important role in accurate runoff forecasting (Beven, 2012). A failure to consider the complex changes in soil surface microtopography may lead to large errors in the soil erosion model according to Wu et al. (2019). However, in current laboratory experiments, the duration of rainfall is short, the scale of soil flume is small, and the soil surface cannot form obvious topographic characteristics, such as rills (Aksoy et al., 2016). In general, there is no distributed modelling method that can reflect complex gully networks and slope shapes and provide the errors of soil erosion prediction. To date, no consensus has been reached on the spatial structure of rills and slopes in terms of rainfall, runoff and soil erosion (Wu et al., 2017, 2019), hindering the further development of targeted soil conservation strategies that take spatial variability into account.

In this study, we propose a new model, namely, a soil erosion model coupled with hydrodynamics and the Green-Ampt (G-A) model, for simulating soil erosion to improve the understanding of the interaction between rainfall and soil erosion. Theoretically speaking, water flow on a slope is a complex three-dimensional water flow problem. Therefore, it is not appropriate to apply the traditional shallow water equation (SWE) to describe the water flow on a steep slope. It should be noted that the model established in this study is not suitable for steep slopes or uneven terrain. The developed model uses graphic processing unit (GPU)-based acceleration technology when solving the numerical model, which accelerates the computational efficiency. With the use of simulations of soil erosion, transport and deposition on slopes and small watersheds, the spatial distribution characteristics of soil erosion caused by rainfall can be evaluated.

## 2 Modelling approach and development

Based on the spatial and temporal dynamic model coupling physical and empirical laws, we design a model including soil infiltration, erosion and sediment transport modules to provide directions for further solving the 2D sediment transport equation.

We calculate the overland flow by using 2D SWEs, which include one continuity equation and two equations of motion of coordinate directions  $x$  and  $y$ . The rainfall energy is the essence of sediment detachment, and the runoff energy is the conveyer energy for eroded sediment. Raindrops can increase the solute transport process from soil into surface runoff, and separated substances may be transported because of the interaction of raindrops and water alone or in

combination. When suspended sediment is no longer supported by water, the sediment is deposited due to the decrease in water transport capacity.

Assuming that the initial soil layer is dry, rainfall should be considered in the model. In this case, the flow depth, velocity and sediment concentration at the calculated point are converted to the boundary condition being set to zero during the calculation in the model. In addition, the soil surface may become dry again after rainfall events. As a result, numerical complexity requires specific program to resolve. One case involves a very shallow water inrush, in which the speed requires special treatment (Hou et al., 2013a, b). The corrected program in the next time step uses the wetting/drying front and necessitates implementing a negative water depth method flexibly according to the need (Hou et al., 2013a, b). The numerical model is represented as a square divided in a uniform grid with longitudinal and transversal slopes in the  $x$  and  $y$  directions of the physical domain. These directions are represented by the upper end with a closed boundary and the lower end with an open boundary. Based on the rectangular grid, we couple the sediment transport module on the basis of the hydrological hydrodynamic numerical model, and establish a 2D water-sediment coupling model on the slope under the moving bed condition by using the finite volume method, which is used to simulate the unsteady flow of water and the transport of viscous sand in the process of slope erosion.

This is a fully coupled model of water and sediment that considers the influences of sediment density and topography on flow movement. The central upwind scheme is used to solve the interface flux, and the linear reconstruction of the interface variable is incorporated to ensure second-order spatial accuracy. The model uses the unbalanced sediment transport formula to calculate the sediment transport process. In the entire calculation process, the model can ensure that the calculated water depth is nonnegative and has strong stability and robustness. The erosion rate is considered to be positive under detachment and negative under deposition. The soil detachment rate increases with increasing flow shear stress, upon which the flow shear stress that acts on the soil exceeds the critical shear stress, and rill detachment can be predicted.

## 2.1 Hydrology model of soil infiltration

The approximate stagnant water model was proposed based on capillary theory (Green and Ampt, 1911) and was termed the G-A infiltration model (Chu, 1978). In view of the advantages of the simple form of the G-A model, it has been improved under specific conditions for ease of application. The governing equation is as follows:

$$f_p = \begin{cases} R & t \leq t_p \\ K_s [1 + (\theta_s - \theta_i) S_f / I_p] & t > t_p \end{cases}, \quad (1)$$

where  $f_p$  represents the instantaneous infiltration rate ( $\text{cm/s}$ );  $R$  represents the rainfall intensity ( $\text{cm/min}$ );  $K_s$  represents the saturated vertical hydraulic conductivity ( $\text{cm/min}$ );  $\theta_i$  and  $\theta_s$  are the initial water content of soil and saturated water content ( $\text{cm}^3/\text{cm}^3$ ), respectively;  $S_f$  is the humid front suction ( $\text{cm}$ );  $I_p$  represents the cumulative infiltration after ponding ( $\text{cm}$ );  $t$  represents the time ( $\text{min}$ ); and  $t_p$  is the time to ponding ( $\text{min}$ ).

The function  $t_p$  is defined as:

$$t_p = \frac{I_p}{R}. \quad (2)$$

## 2.2 Soil erosion sediment transport submodule

As an effective approximation of Saint Venant's equation (Hou et al., 2020), the governing equation uses the 2D SWEs of Equation 3, including the vertical average. We assume that pressure distribution of hydrostatic Reynold's average, viscosity and turbulent pressure are not taken into account. The equation is expressed as follows to ensure the conservation of its format (Chen et al., 2013):

$$\frac{\partial q}{\partial t} + \frac{\partial F}{\partial x} + \frac{\partial G}{\partial y} = S, \quad (3)$$

in which:

$$q = \begin{bmatrix} h \\ q_x \\ q_y \\ hc \\ z_b \end{bmatrix}; \quad F = \begin{bmatrix} q_x \\ uq_x + \frac{gh^2}{2} \\ uq_y \\ \frac{1}{\beta}q_x C \\ 0 \end{bmatrix}; \quad G = \begin{bmatrix} q_y \\ vq_y + \frac{gh^2}{2} \\ vq_x \\ \frac{1}{\beta}q_y C \\ 0 \end{bmatrix}; \quad S = \begin{bmatrix} R \\ S_{bx} + S_{fx} \\ S_{by} + S_{fy} \\ E - D \\ \frac{D - E}{1 - P} \end{bmatrix}, \quad (4)$$

$$S_b - \frac{\partial h}{\partial s} = S_f, \quad (5)$$

$$R = i \cos \gamma - f_p, \quad (6)$$

$$q_x = q \cos \alpha_f, \quad (7)$$

$$q_y = q \sin \alpha_f, \quad (8)$$

where  $q$  represents the flow variable vector that consists of  $\eta$ ;  $F$  and  $G$  are the flux vectors of the conserved variables in the  $x$  and  $y$  directions, respectively;  $S$  represents the source vector;  $h$  is the flow depth (m);  $q_x$  and  $q_y$  are the unit-width discharge values in the two Cartesian directions ( $m^2/s$ );  $h$  is the flow depth (m);  $c$  is the volumetric concentration in sheet flow layer (dimensionless);  $z_b$  is the bed elevation (m);  $\beta$  denotes the velocity difference between sedimentary facies and fluid water (Greimann et al., 2008), which equals 1 (Guan et al., 2014);  $v$  is the average flow velocity in  $y$  direction (m/s);  $C$  is the volumetric concentration in flow depth (dimensionless);  $P$  is the sediment material porosity (dimensionless);  $S_b$  represents the bed slope in source terms;  $S_f$  represents the friction slope in source terms;  $i$  is the rainfall intensity (m/s);  $f_p$  is the infiltration rate through the soil surface (cm/s);  $\gamma$  is a coefficient;  $\alpha_f$  is the angle between  $S$  and  $x$  ( $^\circ$ );  $g$  is the gravitational acceleration ( $m/s^2$ );  $D$  is the sediment deposition rate, and it can be calculated by  $D = \omega_s C_a$ , where  $\omega_s$  represents the sedimentation velocity of sediment particles (m/s), and  $C_a$  is the near-bed equilibrium concentration at the reference level; and  $E$  is the sediment stripping rate, which can be calculated by  $E = \omega_s C_{ae}$ , where  $C_{ae}$  is the balanced near-bed sediment concentration at the reference height level (Smith and Mclean, 1977).

### 2.3 Numerical scheme

In this study, based on the finite volume method in the Godunov format, we use the Harten-Lax-van Leer contact (HLLC) approximate Riemann solver to obtain the coupled solution of the water flow and solute transport flux. In all the test cases considered in this work, two types of boundary conditions, i.e., an open boundary and a closed boundary, are used. The boundary conditions are controlled by flux calculations at the boundary (Hou et al., 2013a, b). The solute advection process simulation adopts the second-order explicit total variation diminishing (TVD) scheme with a limiter to control the numerical error, which reduces the numerical dissipation and numerical oscillation caused by the advection term of the transport equation; the implementation is detailed in the preliminary work (Horton, 1993; Hu and Cao, 2009; Liang and Marche, 2009; Hou et al., 2013a, b, 2015).

Additionally, the running time on a specific computing device is often used to quantitatively evaluate the computational efficiency of a numerical model. The computing device configuration used is an Intel i7-6700 central processing unit (CPU) running at 3.40 GHz with a Windows 10 operating system. The C++ (C++ Programming) and CUDA (Computer Unified Device Architecture) languages are used to program the GPU-based accelerated parallel computing process. In CUDA programming, the CPU is used as the host, and the GPU is used as the coprocessor. The CPU is responsible for processing logical transactions and serial operations, and the GPU is responsible for performing parallel computing tasks. First, the data are read into the

CPU, and the grid information, boundary conditions and calculation parameters are initialized in each grid. Then, the data are allocated to the corresponding GPU device space, and the data are copied to the GPU memory. After the calculation is completed, the results are synchronized with the CPU.

### 3 Model verification

The evaluation data of the model set are performed at the State Key Laboratory of Soil Erosion and Dryland Farming on the Loess Plateau, Northwest A&F University, Shaanxi Province, China (Liu et al., 2006). The experimental parameters of the pan include a slope length of 3.2 m, a width of 1.0 m, a depth of 0.3 m and a slope of 20°. The artificial rainfall is produced with a side-spray automatic rainfall simulation system. The nozzle height is approximately 16.0 m, the rainfall uniformity is greater than 90%, and the rainfall intensity could be controlled in the range of 150–200 mm/h. In the experiment, the artificial filling method is used. Local loess with a thickness of 25 cm is evenly laid in the groove, and the median particle size is approximately 0.02 mm. The volumetric density of the soil is 1.33 g/cm<sup>3</sup>, the initial soil water content is 0.2206 cm<sup>3</sup>/cm<sup>3</sup>, and the saturated water content is 0.5027 cm<sup>3</sup>/cm<sup>3</sup>. In this experiment, the soil effective water conductivity is 1.67×10<sup>-6</sup> m/s, and the matric suction is 0.15 m. When rainfall runoff is generated, a sample is taken every other time, and the beaker volume is 300 mL each time. The sampling time is recorded with a stopwatch. The instantaneous runoff flow and sediment concentration are determined by the drying method, and then, the cumulative runoff volume and erosion amount are approximated (Liu et al., 2006).

Figure 1 represents the relationships of time with runoff velocity, flow discharge and cumulative erosion amounts. In the first 10 min, with the time increasing, the simulated value of the average flow velocity shows the same sharp increasing trend as the measured value. After 10 min, the value gradually shows a steady trend. The average flow velocity value remains at approximately 0.23 m/s, which is higher than the measured value. The value is slightly larger and lasts until 50 min, and the simulated value and the measured value tend to be similar. The flow rate change also shows the same trend as the flow rate. As time increases, the flow rate shows a sharp increasing trend. With the accumulated sediment yield increases over time, the simulated value and the measured value show the same trend, which is basically the same. Overall, the average velocity and flow rate increase with increasing time, and finally, the cumulative sediment yield increases, which is in line with the physical mechanism of erosion and sediment yield. The simulated values of flow velocity, flow discharge and cumulative erosion are closer to the measured values, which shows that the experimental and simulated values have the same change trend, indicating a good agreement between them.

Overall, the simulated results of the flow velocity, flow discharge and cumulative erosion show that the model can reproduce the changes in the rainfall runoff process and erosion, and the capability allows efforts of erosion modelling to also be extended to slopes by using the method.

To quantitatively analyze the simulation results, this study uses three indicators, including root mean square error (RMSE), coefficient of determination ( $R^2$ ) and mean relative error (MRE) to evaluate the model effect. These three parameters can be defined as follows:

$$\text{RMSE} = \sqrt{\frac{\sum_{i=1}^n (M_i - S_i)^2}{N}}, \quad (9)$$

$$R^2 = \frac{\left| \sum_{i=1}^n (M - \bar{M})(S - \bar{S}) \right|^2}{\sum_{i=1}^n (M_i - \bar{M})^2 \sum_{i=1}^n (S_i - \bar{S})^2}, \quad (10)$$

$$\text{MRE} = \frac{1}{n} \sum_{i=1}^n \frac{|S_i - M_i|}{M_i}, \quad (11)$$

where  $M$  is the measured value;  $S$  is the simulated value;  $\bar{M}$  is the mean measured value;  $\bar{S}$  is

the mean simulated value; and  $n$  is the sample number. The closer the  $R^2$  is to 1, the closer the result is to the exact solution. The closer the RMSE is to 0, the closer the result is to a perfect fit.

As shown in Table 1, the proposed model is shown to be reliable in simulating slope soil erosion and can obtain good slope morphology prediction results. The comparative analysis shows that RMSE,  $R^2$ , and MRE can also reflect the accuracy of the simulation results. Therefore, the prediction model constructed in this study has strong advantages.

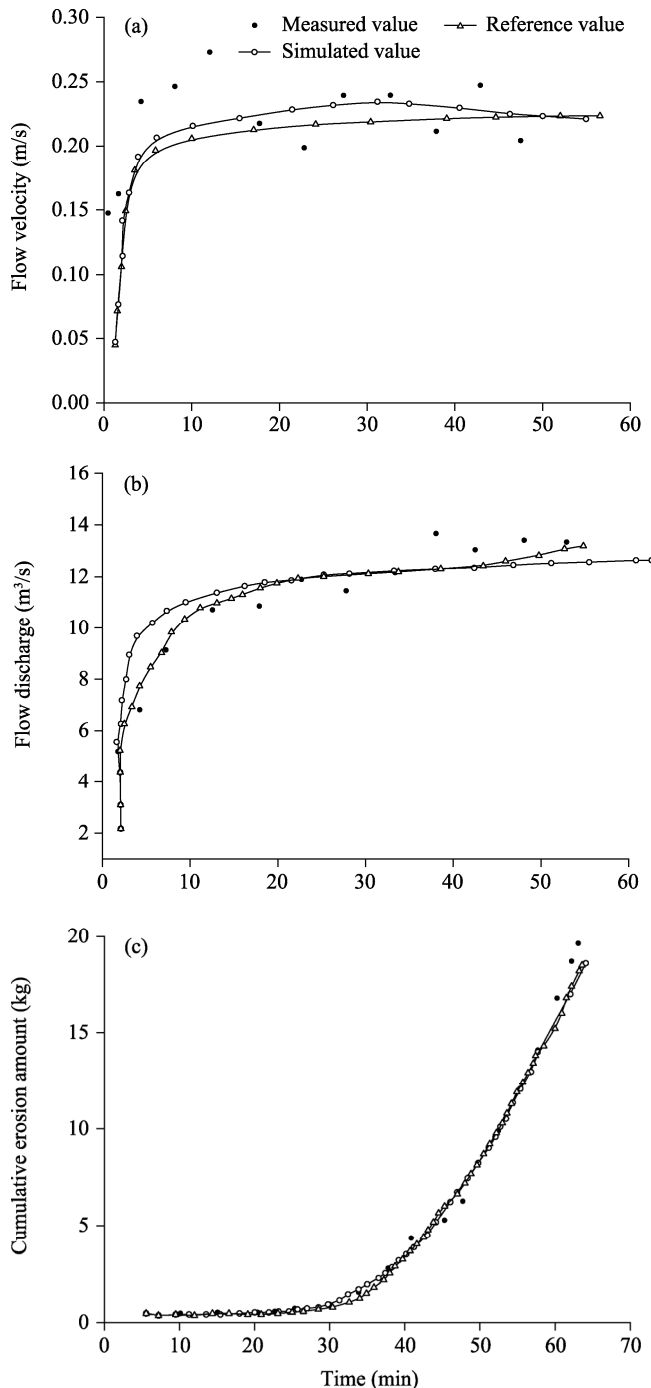


**Fig. 1** Relationships between flow velocity and time (a), between flow discharge and time (b), and between cumulative erosion amount and time (c)

**Table 1** Performance evaluation indices of the model developed in this study

Parameter	RMSE	$R^2$	MRE
Flow velocity	0.152	96.5	1.395
Flow discharge	0.059	94.1	1.208
Cumulative erosion	0.037	90.2	1.433

Note: RMSE, root mean squared error;  $R^2$ , coefficient of determination; MRE, mean relative error.

## 4 Results and discussion

### 4.1 Numerical simulation example of an indoor slope

The first case chosen to test this model is a slope erosion test under artificial rainfall conditions (Wang et al., 2018). The experiment is conducted in the Rain Test Hall of the State Key Laboratory of Ecological Water Conservancy Engineering in Northwest Arid Areas, Xi'an University of Technology, Shaanxi Province, China. The test adopts an adjustable slope steel channel, with the slope of 15° and the test scale of 6.0 m×1.5 m×0.6 m (length×width×depth) (Wang et al., 2018). To simulate the water permeability characteristics of natural soil, we arrange seepage holes at the bottom of the sink. The test soil samples are taken from the local loess soil in Ansai District (36°45'N, 109°11'E) of Shaanxi Province, and the samples are then air-dried. Soil particle components are shown in Table 2.

**Table 2** Particle components of the experimental soil

Soil type	Particle percentage (%)						
	>1.000 mm	0.250–1.000 mm	0.050–0.250 mm	0.010–0.050 mm	0.005–0.010 mm	0.001–0.005 mm	<0.001 mm
Loess	0.00	1.30	32.80	46.70	2.90	5.80	10.50
Natural sand	0.00	62.18	24.60	11.95	1.27	0.00	0.00

In the procedure, we cover the loess with 20 cm of natural sand, and control the average dry volume of the soil at 1.09 g/cm<sup>3</sup>. Clay loess is used to quantify the effects of runoff and sediment from the upper slope on downslope rill erosion and sediment under different sediment concentrations and rainfall intensities. We simulate continuous rainfall with a downward rainfall sprinkler system. The total test rainfall time is 60 min, and the designed rainfall intensity is 50 mm/h. After rainfall erosion starts, sediment samples are collected under the water tank at an interval of 5 min.

Under the action of rainfall and runoff, the erosion evolution of rills on slopes can be divided into the following three processes. First, under the action of rainfall, runoff gradually forms and flows along rills. Second, as the water flow transports erode soil particles, the uneroded rill sidewalls collapse under the action of a shearing force. Third, the erosion of the toe from the sidewall of the rill groove starts suddenly and unpredictably because of the gravity. In addition, while small narrow grooves form, cracks also form on the side surfaces of the narrow grooves due to the action of the shearing force. When gravity is greater than the cohesion and friction of the soil, small collapses occur to form rills. Martinez-Casasnovas et al. (2004) and Chen et al. (2013) found that under the continuous repetition of rainfall and currents, the overhanging layer continues to be destroyed by rapid concentrated flow, leading to the acceleration of collapse and gully erosion.

The specific process is described as follows. As shown in Figure 2a, at  $t=0$  s (where  $t$  is the time), as the rainfall time increases, runoff starts and gradually forms, and rills also form on the slope. Over the period of  $t=10$ –50 s, with the gradual formation of runoff, the runoff velocity of the slope rapidly increases, but the runoff energy consumed by the soil erosion process gradually decreases at the bottom of the slope and is accompanied by the formation of rills. During the period of  $t=100$ –1000 s, with the gradual widening and scouring of the sidewalls of the slope rills,

erosion channels are formed, sand particles begin to be transported, which presents small rills one by one, and the shape of the entire slope changes. As shown in Figure 2, these three processes accordingly promote and influence one another within this time. Comparatively, the change in the flow depth between rills is small in terms of soil erosion. As shown in Figure 2c-d, the changes in space are easily detectable over the period of  $t=100\text{--}1000\text{ s}$ , mainly because the strength of rill erosion primarily depends on the rainfall intensity and rainfall duration. The area with strong slope erosion is in the middle part because of the strong erosion ability at this location. Although the slope length is the same, the erosion intensity varies greatly in different rills. For slopes with greater continuity and larger inclination angle, the runoff velocity and erosion capacity are larger.

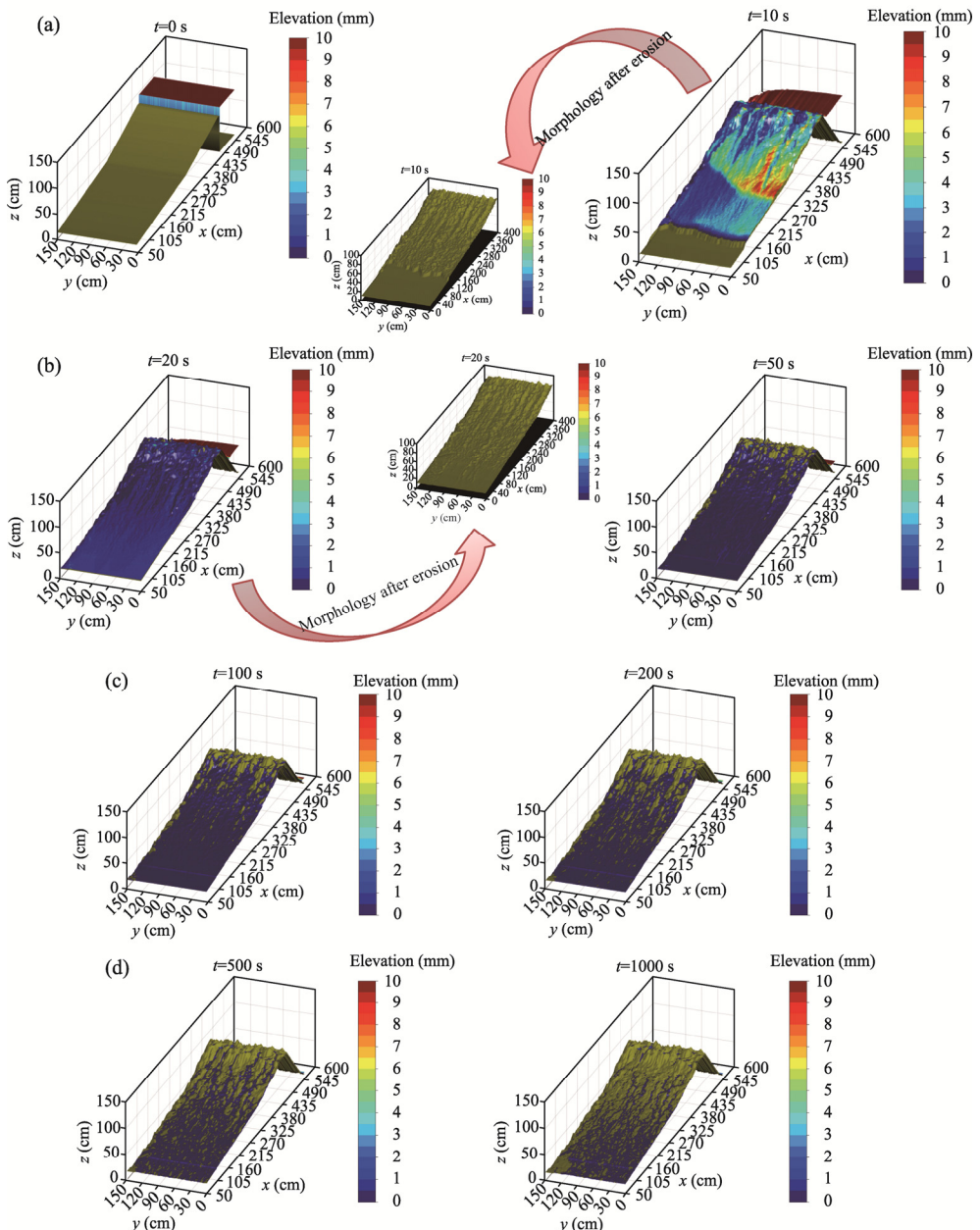


**Fig. 2** Accumulation of slope erosion at different times. (a), 0 and 10 s; (b), 20 and 50 s; (c), 100 and 200 s; (d), 500 and 1000 s.

In the actual field environment, the length of the slope usually ranges from several metres to nearly hundreds of metres, and the slope changes are also different. The seasonal distribution of precipitation is highly uneven, and the intensity of rainstorms is also very different. Most rainstorms have short durations and uncertain locations (Wang and Jiao, 1996; Jiang, 1997). Accordingly, these extreme differences in topography and rainfall can also lead to different characteristics of slope soil erosion. Rainfall is often random and uneven, and the variation in intensity has different impacts on slope soil erosion. Some scholars have studied the influences of different rainfall patterns on slope soil erosion (Cerdà et al., 2017). Under the same rainfall intensity, with the passage of time, the permeability becomes increasingly lower and more stable, and the excess rainfall rate also increases. This is because when the rainfall peak is later, the runoff erosion capacity at the peak time is higher (Liu et al., 2006).

Furthermore, the erosion between the slope rills does not change continuously, because each grid element is connected to others in the  $x$  or  $y$  direction in the modelling process. The slope gully is susceptible to major pattern changes and substantial shifts as the slope gully is eroded, transported, and deposited, where the sediment load and water to discharge may change. The gradient in the  $y$  direction on each grid is steeper than the gradient in the  $x$  direction. Therefore, the soil is more easily eroded in the vertical direction, that is, in the  $y$  direction of the grid.

As shown in Figure 3, the sediment yield and rill erosion width show an overall upward trend over time. The sediment yield and rill erosion width have very similar trends over time, and the time 800 s is the turning point when the rill erosion width begins to be greater than the sediment yield rate. The reason may be that the source of sand production on the slope has changed. The regression analysis results show that the cumulative sediment yield and rill erosion width have an extremely linear positive relationship:

$$Y = aX - b, \quad (12)$$

where  $Y$  is the cumulative sediment yield (g);  $X$  is the rill erosion width (mm); and  $a$  and  $b$  are the undetermined coefficients, with the values of 0.8743 and 2.4012, respectively. In this study, a prototype rill is constructed along the flow direction in the middle of the slope to guide the development of the rill structure by assuming its width is 2.4012 mm. Therefore, in the case of different slope lengths and grades, modelling is carried out according to the actual situation.

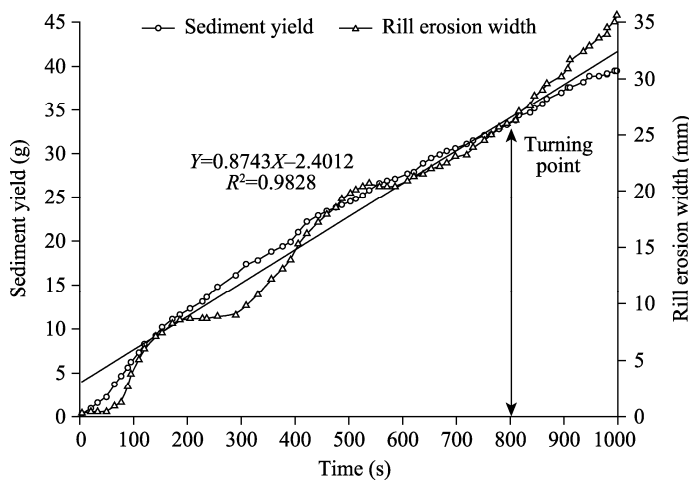


**Fig. 3** Relationship between sediment yield ( $Y$ ) and rill erosion width ( $X$ ) at different times

As shown in Figure 4, the runoff velocity over time shows a downward trend; at test times of 0–100, 100–140, and 320–510 s, the runoff velocity exhibits four sharp decreases. Two of the rapid decreases in the runoff velocity correspond to the two rapid increases in the narrow groove width. However, in the two phases at the beginning and end of the experiment, the changes in the flow rate of the concentrated water flow and the width of the rill are not consistent. In the first 100 s of the test experiment, the runoff velocity is reduced by 40.0%, while the width of the rill

remains unchanged. The main reason is that the shearing force of concentrated water on the ditch toe greatly increases the runoff width and reduces the runoff depth, so that the runoff velocity is reduced and the ditch foot wash-out height decreases with the increasing wash-out depth. Over 320 to 360 s, the width of the narrow groove increases by 17.0%, while the flow rate of concentrated water flow decreases by only 9.5%. Under the condition that the erosion rate of the ditch foot wash-out caused by the runoff shearing force is essentially unchanged, more ditch wall expansion and invasion occur.

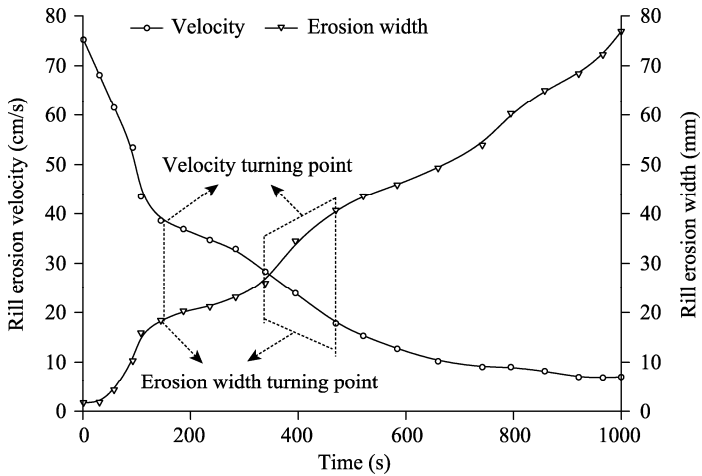


Fig. 4 Variations of rill erosion velocity and rill erosion width with the passage of time

The regression analysis results shown in Table 3 reflect that there is a significant negative correlation between runoff velocity and rill erosion width, which can be expressed by an exponential function:

$$Y=104.12e^{-0.051X} \quad (R^2=0.9591, P<0.005), \quad (13)$$

where  $Y$  is the runoff velocity (cm/s) and  $X$  is the width of the narrow groove (cm).

The applicability and accuracy of the GAST (GPU Accelerated Surface Water Flow and Transport Model) in the study area can be determined by  $R^2$  and  $E_{NS}$  indicators for evaluation.  $R^2$  is calculated by a linear regression between the measured value and the simulated value to represent the simulation consistency level of the change trend between runoff and measured flow.  $E_{NS}$  represents the similarity between the simulated value and the measured values at the 1:1 level. For example,  $E_{NS}=0.8$  means that 80% of the simulated values are similar to the measured values. The calculation formula of  $E_{NS}$  is as follows:

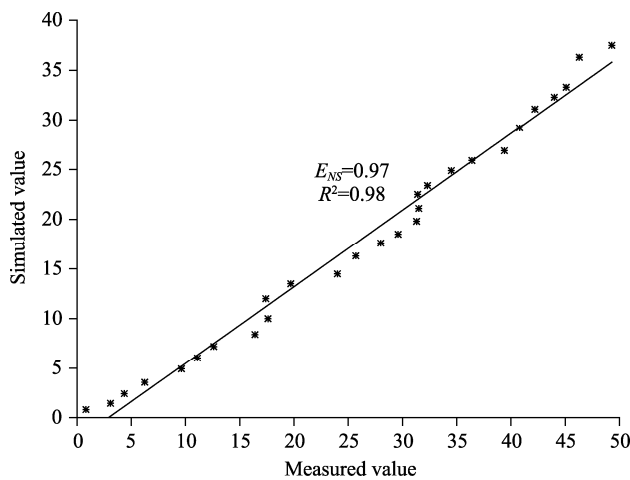
$$E_{NS}=1-\frac{\sum_{i=1}^n(O-M)^2}{\sum_{i=1}^n(\bar{O}-\bar{M})^2}. \quad (14)$$

In the formula,  $M$  is the actual measured value,  $O$  is the model simulated value,  $\bar{M}$  is the average of the actual measured values,  $\bar{O}$  is the average of the simulated values, and  $n$  is the number of observation data points.

As shown in Figure 5, the high-efficiency and high-resolution numerical model based on GPU-based acceleration technology that couples hydrodynamics and morphology established in this study has been indicated to be reliable and has achieved good results in simulation prediction. The calculation results show that the  $R^2$  and  $E_{NS}$  values are 0.97 and 0.98, respectively. Therefore, the erosion prediction model established in this study shows a strong and broad general type, which reflects that the model can well simulate the spatial distribution characteristics of inter-ditch erosion.

**Table 3** Erosion rill velocity and width at different times

Time (s)	Erosion rill velocity (cm/s)	Erosion rill width (mm)
1.36	75.20	1.74
30.90	68.10	1.79
58.10	61.50	4.31
93.00	53.40	10.30
108.00	43.50	15.90
145.00	38.60	18.40
187.00	36.90	20.30
236.00	34.70	21.20
284.00	32.90	23.10
339.00	28.30	26.00
395.00	23.90	34.50
470.00	17.80	40.70
521.00	15.30	43.60
584.00	12.70	45.90
660.00	10.20	49.30
742.00	9.02	53.90
795.00	9.04	60.30
858.00	8.20	65.00
921.00	6.99	68.40
966.00	6.89	72.20
1000.00	7.02	76.90

**Fig. 5** Correlation between the simulated and measured rill erosion values

#### 4.2 Numerical simulation example of the erosion process in a small watershed

The second case chosen to test this model is an experiment of Coquet River Basin that involves watershed erosion (Hou et al., 2020). The associated reaches are chosen because they have considerable historic instability in terms of channel patterns and morphology, and rising river water promotes erosion under rainfall conditions. As shown in Figure 6, the erosion depth changes and erosion cumulative amount of the basin over 1–40 h is simulated. The elevation difference of erosion is on the order of 0.5–3.0 m. The average erosion depth overall increases over time, especially at  $t=20\text{--}30$  h (Fig. 6e–f).

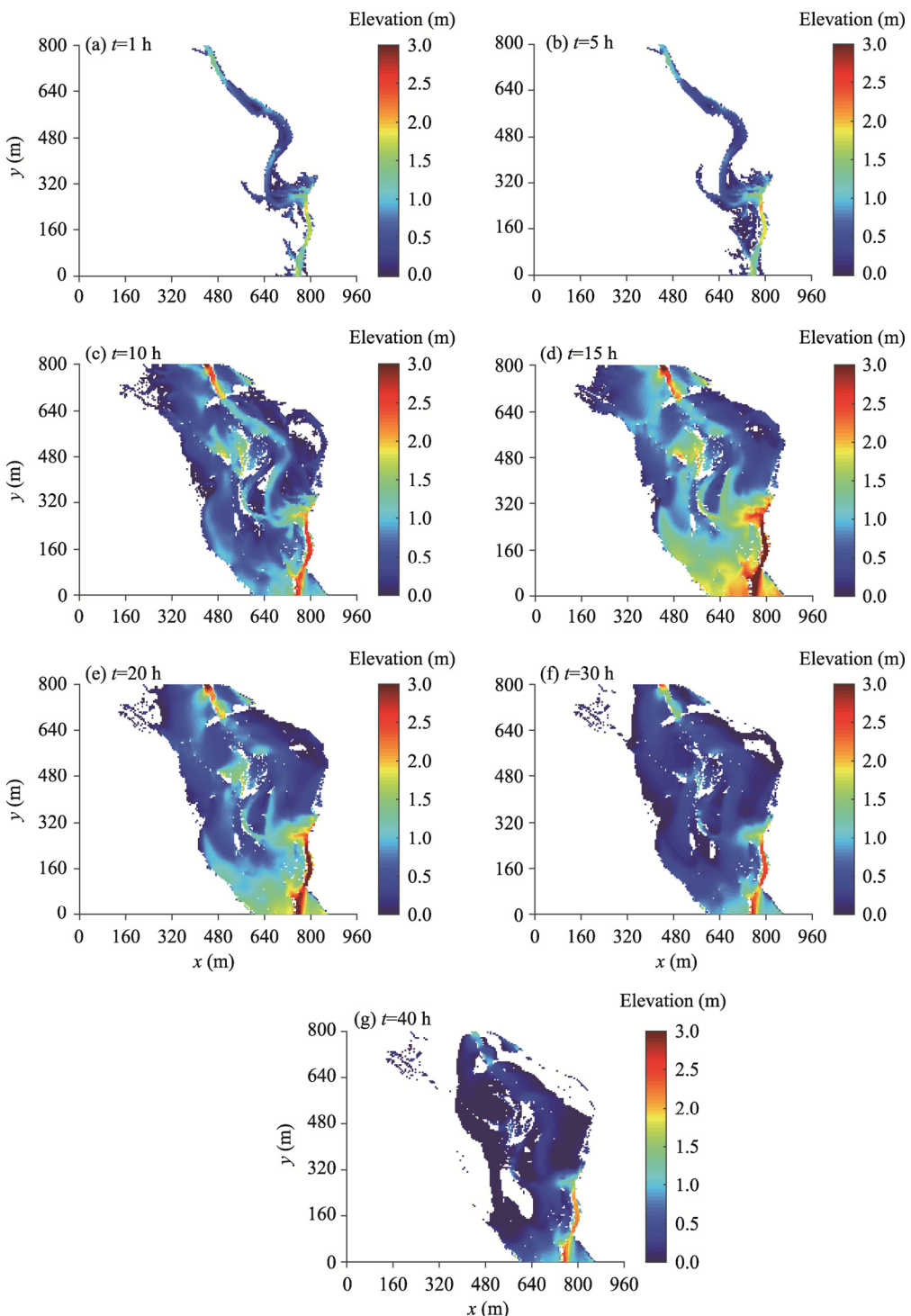


**Fig. 6** Numerical simulation of watershed erosion process of the Coquet River Basin at different times. (a), 1 h; (b), 5 h; (c), 10 h; (d), 15 h; (e), 20 h; (f), 30 h; (g), 40 h.

For significant erosion sites and rainfall events, the key simulation results focus on determining model capabilities and erosion patterns. The results of these simulations appear as hourly outputs (data not shown). Selected important time frames are used to represent the changes in the spatial location of erosion over the entire basin. These results are used to illustrate the morphological

changes of watershed erosion, including sediment erosion and important river sections of deposition, to provide a concept of the relationship between morphological changes and eroded energy (Fig. 7). Due to river erosion and sediment exchange and migration (Ham, 2005), energy seems to concentrate in the riverbed (Fuller et al., 2003). In addition to the large amount of sediment migration that leads to river channel deposition, the river channel migrates again during the relaxation period due to erosion and then redeposits in the lower reaches of the river. The large amount of siltation that occurs in the river section of the river basin is also attributed to the increase in the inflow of sediment at the higher flow rate coupled with the input of river bank erosion, considering that the low slope of the study river section is a key factor that affects the river's response to major floods. This restricts the transport and deposition of coarse bedrock in the upper part (Danks, 1998). Therefore, a low slope leads to decreases in sediment transport capacity and water flow power. Accordingly, the high rate of bank retreat is related to the excessive concentration of flow energy on the bank, leading to greater lateral erosion, especially on the outside of the bend (Newson, 1980; Hickin, 1984).

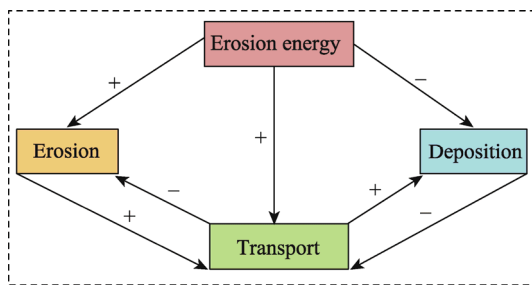


**Fig. 7** Watershed erosion energy exchange. "+" and "−" indicate positive and negative work done, respectively. Positive work corresponds to erosion and negative work to deposition.

As shown in Figure 8, a total of nine cross sections of the Coquet River Basin are considered for the measured old riverbed and simulated new eroded riverbed analysis. By analysing the conditions of each section, we can better understand the changes of the topography of the river section that are most affected by different erosion intensities and key deposition processes, as well as their influencing factors. Based on the results of a series of cross sections, the more stable subranges are more resistant to morphological changes and sediment flux, and these subranges have not yet undergone fundamental landform changes in response to high-intensity erosion. In terms of erosion sediment mobility, there are strong responses to high-intensity erosion or frequent low-amplitude events.

As shown in Figure 8a, when comparing the old riverbed with the new eroded riverbed, at the distance of 20.00 m, the new eroded riverbed is lower than the old riverbed, with a height difference of approximately 0.45 m. This reduction is caused by processes such as strong erosion of the watershed and the "over-transport" of sediments. These processes change the structure of the upper reaches of the basin and transfer a large amount of sediment to the middle and lower reaches of the basin. Similarly, as shown in Figure 8b–i, the erosion change range of the old riverbed and the new eroded riverbed is 0.20–1.00 m. Continuous erosion processes and the increase in the width of the lateral soil erosion lead to the further migration of Cross section 9 (Fig. 8i), and bank retreat can potentially be driven by frequent bank failures on the left-hand bank. This process, also known as cantilever failure, is the progressive removal of riparian material by flow erosion of non-viscous riparian material, which is composed of non-viscous sand.

The quantitative analysis results about the erosion and deposition processes of riverbed at the nine cross sections of the Coquet River Basin are shown in Figure 9. In the most severely eroded area, the erosion depth is approximately 13.00 m. In general, the degree of erosion for each cross section is greater than that of siltation. The depth of erosion change value ranges from −0.86 to

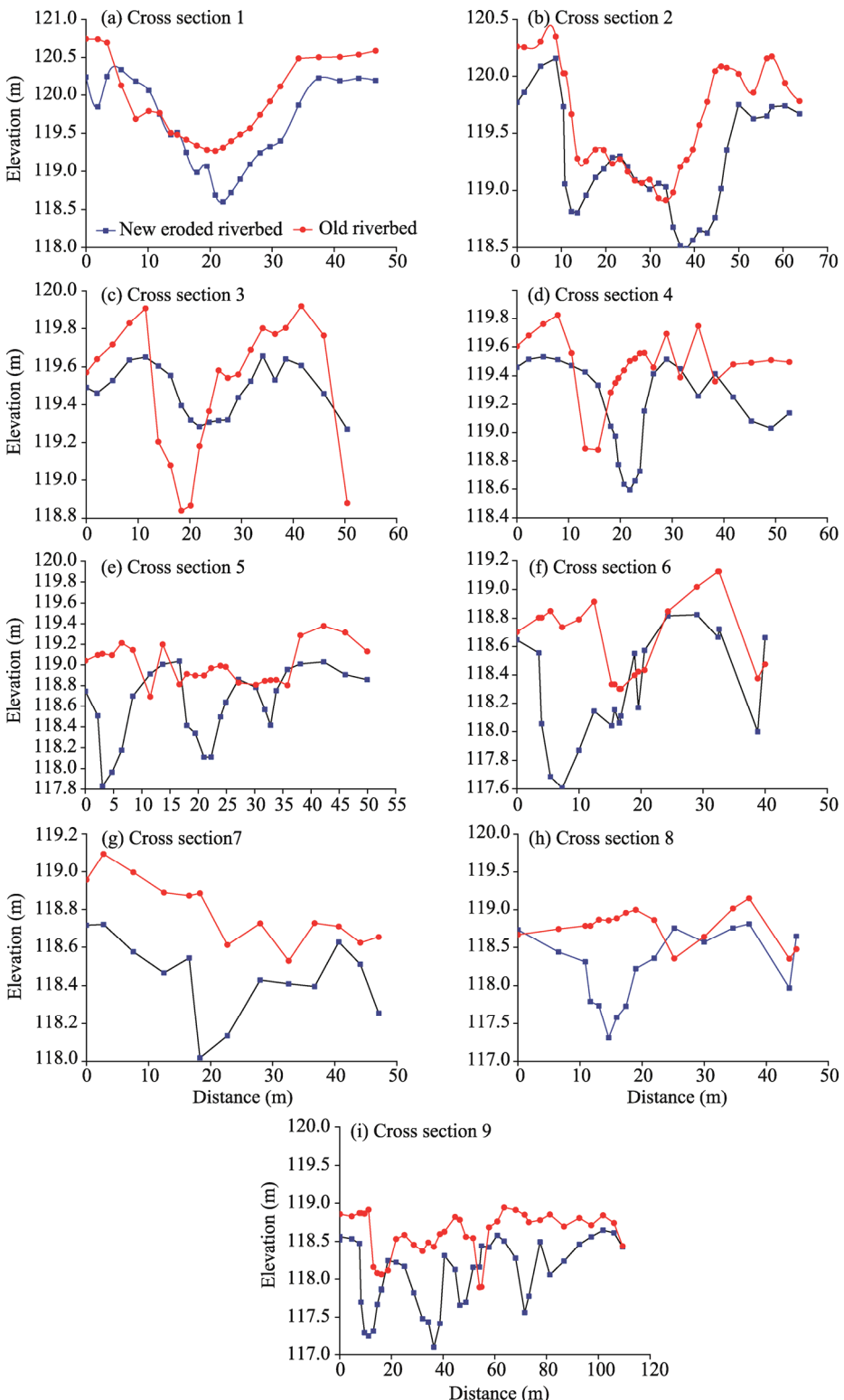


**Fig. 8** Comparisons of elevations for the measured old riverbed and simulated new eroded riverbed at nine cross sections of the Coquet River Basin (a-i)

-2.79 m, and the depth of deposition change value is in the range of 0.38–1.02 m. Normally, the erosion depth of most areas is approximately 1.00 m, mainly in flood-prone regions. We compare

erosion and deposition by calculating the accumulation of sediment in this basin, and find that the overall erosion is net erosion. This illustrates that erosion process dominates the basin in terms of the erosion geomorphological bed and nine cross section profiles, in turn leading to an increase in the width of the basin. Therefore, the process can be regarded as watershed erosion.

For this reason, these changes can be attributed to erosion and deposition, which result in alterations in the river channel course, bed elevation, and replacement due to sediment accumulation and changes in the riverbed gradient. In addition to the lateral development of the river course, the bends of the upstream river are eroded, increasing the depth of that particular section of the riverbed. The erosion depth at the Cross section 3 is 2.40 m. The erosion depth at the Cross section 4 is 1.29 m, and the erosion depth at the Cross section 6 is 0.63 m. As a result, the aforementioned factors clearly affect the active channel, particularly by altering the width and gradient of the channel, in addition to the consequential bank erosion. Thus, the eroded channels can be eroded into new channels during the aforementioned reciprocating erosion process and change their width and slope, thus enhancing the erosion process.

Erosion and deposition of the riverbank characterize the basin, as determined by calculating the changes in the balance of erosion and deposition over the period for cross sections 1–9 (Fig. 9) in the basin. The net sediment gains and losses during this period indicate an excess of sediment erosion and the export of material downstream from the reach, which can also occur in stable rivers. This process is also linked to sediment distribution. Generally, the increase in sediment flux is associated with higher rainfall magnitude in conjunction with the sediment input of erosional bank processes, which lead to changes in watershed geometry. Estimating the riverbed and riverbank material erosion along the basin channel may provide an indication of the dominant processes that influence morphologic change and the development of the meandering basin. Consequently, if the eroded sediment is not removed or transported, then a change can be expected in the shape and form of a cross section related to the active basin width.

To demonstrate the performance of the GPU code calculation efficiency, we use a model of CPU (CPU with four cores (Intel Xeon E5-2609/CPU)) calculation to simulate the same test case. The runtime uses different grid resolutions on different hardware devices. As the grid becomes finer, the performance of the GPU code in terms of computational efficiency improves. Therefore, in soil erosion events, GPU acceleration can achieve large-scale simulation calculations and play a great role in the evaluation of water and soil loss processes.

## 5 Conclusions

This study develops a new soil erosion model that couples 2D hydrodynamics and the G-A rainfall infiltration model. The model also applies GPU-based acceleration technology to increase the calculation speed. The model tested shows that its simulation values and measured values indicate a good consistency, and the slope erosion patterns and spatial distribution characteristics at different times are highly consistent with the final ravine shape. It is possible to make good predictions of slope erosion using this developed model. A linear function can be used to predict the amount of sediment transport and the width of rill erosion in slope soil erosion. The rate of erosion depends mainly on the resistance of the soil to corrosion. There are two turning points in the erosion rate and rill erosion width. When the velocity is sharply reduced, the erosion width gradually increases, and when the two reach an equilibrium point, the erosion width gradually decreases as the velocity increases. Notably, the width of the erosion rill depends mainly on the formation and development of the groove opening from small to large. The effect of the shearing force, although small, cannot be ignored. In large-scale basins, bank incisions collapse from small to large, resulting in a large area of riverbank to be eroded and washed away.

## Acknowledgements

This research was funded by the National Natural Science Foundation of China (52079106, 52009104, 51609199) and the National Key Research and Development Program of China (2016YFC0402704). We also thank the anonymous reviewers and editors for their constructive comments for this manuscript.

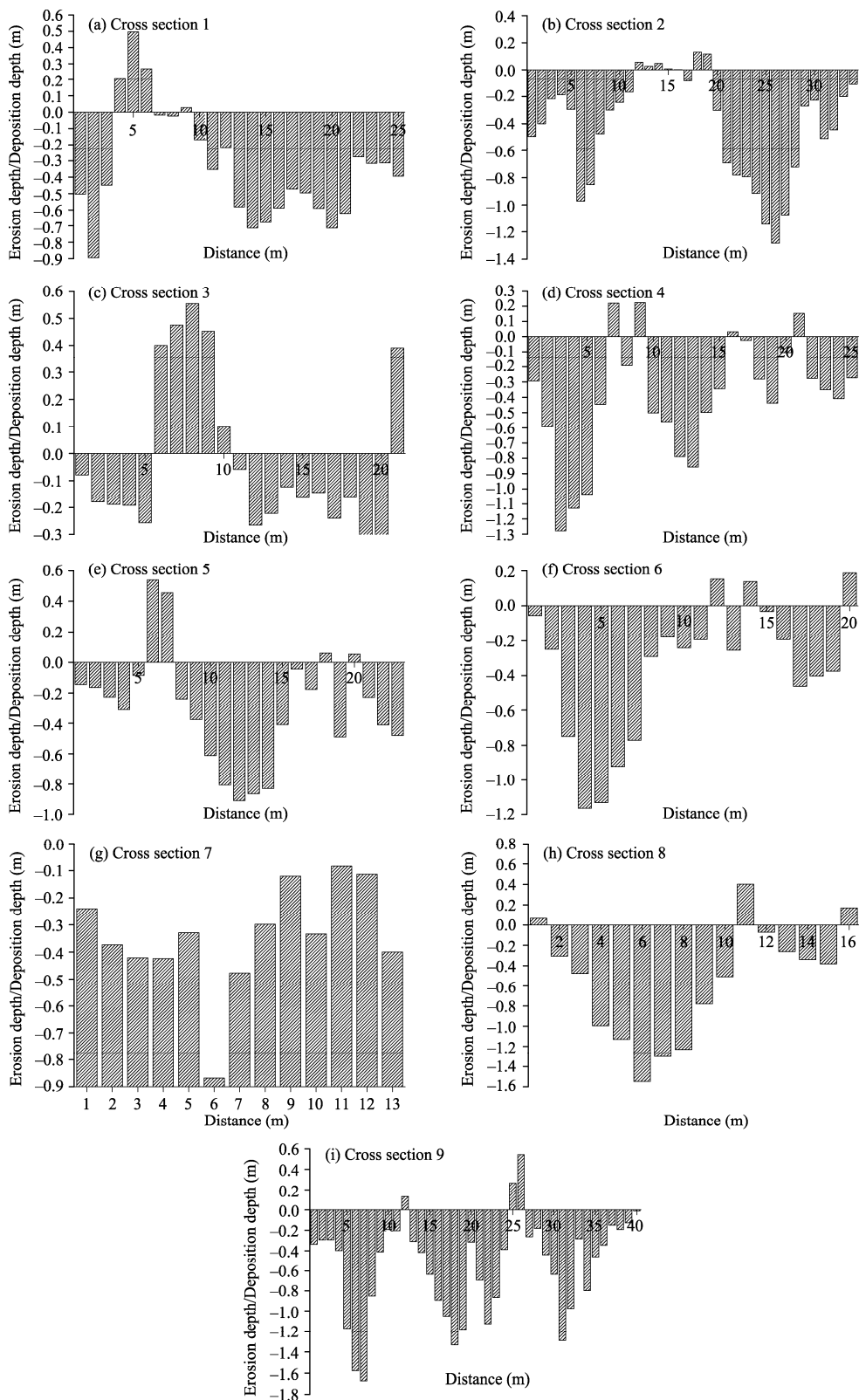


**Fig. 9** Erosion and deposition depths of riverbed at nine cross sections in the Coquet River Basin. The positive and negative values are expressed as deposition depth and erosion depth, respectively.

## References

- Abderrezak K E, Die Moran A, Mosselman E, et al. 2013. A physical, movable-bed model for non-uniform sediment transport, fluvial erosion and bank failure in rivers. *Journal of Hydro-environment Research*, 8(2): 95–114.
- Aksoy H, Gedikli A, Unal N E, et al. 2016. Rainfall runoff model considering microtopography simulated in a laboratory erosion flume. *Water Resources Management*, 30(15): 5609–5624.
- An J, Zhang Y Q, Wang Y Y. 2020. Rainstorm pattern effects on the size distribution of soil aggregate in eroded sediment within contour ridge systems. *Journal of Soils and Sediments*, 20(4): 2192–2206.
- An Y, Liu Q Q. 2009. Two-dimensional hillslope scale soil erosion model. *Journal of Hydrologic Engineering*, 14(7): 690–697.
- Appels W M, Bogaart P W, van der Zee S E. 2011. Influence of spatial variations of microtopography and infiltration on surface runoff and field scale hydrological connectivity. *Advances in Water Resources*, 34(2): 303–313.
- Batista P V G, Davies J, Silva M LN, et al. 2019. On the evaluation of soil erosion models: Are we doing enough? *Earth-Science Reviews*, 197: 102898, doi: 10.1016/j.earscirev.2019.102898.
- Beven K J. 2012. *Rainfall-Runoff Modelling: The Primer* (2<sup>nd</sup> ed.). Chichester: Wiley-Blackwell, 3–15.
- Bingner R L, Wells R R, Momm H G, et al. 2016. Ephemeral gully channel width and erosion simulation technology. *Natural Hazards*, 80(3): 1949–1966.
- Borrelli P, Robinson D A, Fleischer L R, et al. 2017. An assessment of the global impact of the 21<sup>st</sup> century land use change on soil erosion. *Nature Communications*, 8: 1–13.
- Bryndal T, Franczak P, Krocza R, et al. 2017. The impact of extreme rainfall and flash floods on the flood risk management process and geomorphological changes in small Carpathian catchments: a case study of the Kasiniczanka river (Outer Carpathians, Poland). *Natural Hazards*, 88(1): 95–120.
- Cerdà A, Borja M E L, Úbeda X, et al. 2017. *Pinus halepensis* M. versus *Quercus ilex* subsp *Rotundifolia* L. runoff and soil erosion at pedon scale under natural rainfall in Eastern Spain three decades after a forest fire. *Forest Ecology and Management*, 400: 447–456.
- Chaplot V, Brown J, Dlamini P, et al. 2011. Rainfall simulation to identify the storm-scale mechanisms of gully bank retreat. *Agricultural Water Management*, 98(11): 1704–1710.
- Chen A Q, Zhang D, Peng H, et al. 2013. Experimental study on the development of collapse of overhanging layers of gully in Yuanmou Valley, China. *CATENA*, 109: 177–185.
- Chen H, Zhang X P, Abla M, et al. 2018. Effects of vegetation and rainfall types on surface runoff and soil erosion on steep slopes on the Loess Plateau, China. *CATENA*, 170: 141–149.
- Chen L, Sela S, Svoray T, et al. 2013. The role of soil-surface sealing, microtopography and vegetation patches in rainfall-runoff processes in semiarid areas. *Water Resources Research*, 49(9): 5585–5599.
- Chu S T. 1978. Infiltration during an unsteady rain. *Water Resources Research*, 14(3): 461–466.
- Danks M. 1998. Contemporary and historic river channel change at Swinhope burn, Weardale: a study of river response to flood events in an upland, gravel-bed stream. MSc Thesis. Durham: Durham University.
- de Lima J L M P, Santos L, Mujtaba B, et al. 2019. Laboratory assessment of the influence of rice straw mulch size on soil loss. *Advances in Geosciences*, 48: 11–18.
- Di Stefano C, Ferro V, Palmeri V, et al. 2017. Flow resistance equation for rills. *Hydrological Processes*, 31(15): 2793–2801.
- Di Stefano C, Ferro V, Palmeri V, et al. 2018. Testing slope effect on flow resistance equation for mobile bed rills. *Hydrological Processes*, 32(5): 664–671.
- dos Santos J C N, de Andrade E M, Medeiros P H A, et al. 2017. Effect of rainfall characteristics on runoff and water erosion for different land uses in a tropical semiarid region. *Water Resources Management*, 31(1): 173–185.
- Fuller I C, Large A R G, Milan D J. 2003. Quantifying channel development and sediment transfer following chute cutoff in a wandering gravel-bed river. *Geomorphology*, 54(3–4): 307–323.
- González-Hidalgo J C, de Luis M, Batalla R J. 2009. Effects of the largest daily events on total soil erosion by rainwater. An analysis of the USLE database. *Earth Surface Processes and Landforms*, 34(15): 2070–2077.
- Gordon L M, Bennett S J, Wells R R. 2012. Response of a soil-mantled experimental landscape to exogenic forcing. *Water Resources Research*, 48: W10514, doi: 10.1029/2012WR012283.
- Gottardi G, Venutelli M. 1993. A control-volume finite-element model for two-dimensional overland flow. *Advances in Water Resources*, 16(5): 277–284.
- Govindaraju R S, Kavvas M L, Tayfur G. 1992. A simplified model for two-dimensional overland flows. *Advances in Water Resources*, 15(2): 133–141.
- Green W H, Ampt G A. 1911. Studies on soil physics I. The flow of air and water through soils. *Journal of Agricultural*

chinaxiv:202112.00008v1

- Science, 4: 1–24.
- Greimann B, Lai Y, Huang J C. 2008. Two-dimensional total sediment load model equations. *Journal of Hydraulic Engineering*, 134(8): 1142–1146.
- Guan M, Wright N G, Sleigh P A. 2014. 2D process based morphodynamical model for flooding by non-cohesive dyke breach. *Journal of Hydraulic Engineering*, 140(7): 44–51.
- Ham D G. 2005. Morphodynamics and sediment transport in a wandering gravel-bed channel: Fraser River, British Columbia. PhD Dissertation. British Columbia: University of British Columbia.
- Hickin E J. 1984. Vegetation and river channel dynamics. *The Canadian Geographer Le Géographe Canadien*, 28(2): 111–126.
- Horton R E. 1933. The role of infiltration in the hydrological cycle. *Transactions, American, Geophysical Union*, 14(1): 446–460.
- Hou J M, Liang Q H, Simons F, et al. 2013a. A 2D well balanced shallow flow model for unstructured grids with novel slope source term treatment. *Advances in Water Resources*, 52: 107–131.
- Hou J M, Liang Q H, Simons F, et al. 2013b. A stable 2D unstructured shallow flow model for simulations of wetting and drying over rough terrains. *Computers & Fluids*, 82(17): 132–147.
- Hou J M, Liang Q H, Zhang H B, et al. 2015. An efficient unstructured MUSCL scheme for solving the 2D shallow water equations. *Environmental Modelling & Software*, 66: 131–152.
- Hou J M, Kang Y D, Hu C H, et al. 2020. A GPU-based numerical model coupling hydrodynamical and morphological processes. *International Journal of Sediment Research*, 35(4): 386–394.
- Howes D A, Abrahams A D, Pitman E B. 2006. One- and two-dimensional modelling of overland flow in semiarid shrubland, Jornada basin, New Mexico. *Hydrological Processes*, 20: 1027–1046.
- Hu P, Cao Z X. 2009. Fully coupled mathematical modeling of turbidity currents over erodible bed. *Advances in Water Resources*, 32(1): 1–15.
- Jiang D S. 1997. Soil and Water Loss in Loess Plateau and the Regulation Mode. Beijing: China Water & Power Press, 105–110. (in Chinese)
- Liang Q, Marche F. 2009. Numerical resolution of well-balanced shallow water equations with complex source terms. *Advances in Water Resources*, 32(6): 873–884.
- Liu Q, Xiang H, Singh V P. 2006. A simulation model for unified interrill erosion and rill erosion on hillslopes. *Hydrological Processes*, 20: 469–486.
- Martinez-Casasnovas J A, Ramos M C, Poesen J. 2004. Assessment of sidewall erosion in large gullies using multi-temporal DEMs and logistic regression analysis. *Geomorphology*, 58(1–4): 305–321.
- Morgan R P C, Quinton J N, Smith R E, et al. 1998. The European Soil Erosion Model (EUROSEM): a dynamic approach for predicting sediment transport from fields and small catchments. *Earth Surface Processes and Landforms*, 23(6): 527–544.
- Newson M. 1980. The geomorphological effectiveness of floods—a contribution stimulated by two recent events in mid-wales. *Earth Surface Processes and Landforms*, 5(1): 1–16.
- Nord G, Esteves M. 2005. PSEM-2D: A physically based model of erosion processes at the plot scale. *Water Resources Research*, 41: 1–14.
- Panagos P, Katsiyanis A. 2019. Soil erosion modelling: The new challenges as the result of policy developments in Europe. *Environmental Research*, 172: 470–474.
- Qin C, Zheng F L, Xu X M, et al. 2018a. A laboratory study on rill network development and morphological characteristics on loessial hillslope. *Journal of Soils and Sediments*, 18(4): 1679–1690.
- Qin C, Zheng F L, Zhang X C, et al. 2018b. A simulation of rill bed incision processes in upland concentrated flows. *CATENA*, 165: 310–319.
- Renard K G, Foster R, Weesies G, et al. 1997. Predicting soil erosion by water: A guide to conservation planning with the revised universal soil loss equation (RUSLE). USDA Agriculture Handbook 703. Washington, D.C.: United States Department of Agriculture, 1–404.
- Shen H O, Zheng F L, Wen L L, et al. 2016. Impacts of rainfall intensity and slope gradient on rill erosion processes at loessial hillslope. *Soil and Tillage Research*, 155: 429–436.
- Smith J D, Mclean S R. 1977. Spatially averaged flow over a wavy surface. *Journal of Geophysical Research*, 82(12): 1735–1746.
- Smith R E, Goodrich D C, Woolhiser D A, et al. 1995. KINEROS: A Kinematic Runoff and Erosion Model. [2021-04-03]. <https://www.tucson.ars.ag.gov/kineros/>.
- Stroosnijder L. 2005. Measurement of erosion: Is it possible? *CATENA*, 64(2–3): 162–173.
- Sweeney K E, Roering J J, Ellis C. 2015. Experimental evidence for hillslope control of landscape scale. *Science*, 349(6243):

51–53.

- Taye G, Poesen J, Van Wesemael B, et al. 2013. Effects of land use, slope gradient, and soil and water conservation structures on runoff and soil loss in semi-arid northern Ethiopia. *Physical Geography*, 34(3): 236–259.
- Tayfur G. 2007. Modelling sediment transport from bare rilled hillslopes by areally averaged transport equations. *CATENA*, 70(1): 25–38.
- Tian P, Xu X Y, Pan C Z, et al. 2017. Impacts of rainfall and inflow on rill formation and erosion processes on steep hillslopes. *Journal of Hydrology*, 548: 24–39.
- Wang T, Li P, Hou J M, et al. 2018. Response of the meltwater erosion to runoff energy consumption on loessal slopes. *Water*, 10(11): 1522, doi: 10.3390/w10111522.
- Wang W H, Jiao J Y. 1996. Rainfall and Erosion Sediment Yield in Loess Plateau and Sediment Transportation in the Yellow River Basin. Beijing: Science Press, 142–144. (in Chinese)
- Wang Z J, Jiao J Y, Rayburg S, et al. 2016. Soil erosion resistance of "Grain for Green" vegetation types under extreme rainfall conditions on the Loess Plateau. *China. CATENA*, 141: 109–116.
- Wells R R, Momm H G, Rigby J R, et al. 2013. An empirical investigation of gully widening rates in upland concentrated flows. *CATENA*, 101: 114–121.
- Wirtz S, Seeger M, Ries J B. 2010. The rill experiment as a method to approach a quantification of rill erosion process activity. *Zeitschrift Fur Geomorphologie*, 54(1): 47–64.
- Wischmeier W H, Smith D D. 1978. Predicting rainfall erosion losses: A guide to conservation planning. The USDA Agricultural Handbook No. 537. Washington, D.C.: United States Department of Agriculture.
- Woodward D E. 1999. Method to predict cropland ephemeral gully erosion. *CATENA*, 37(3–4): 393–399.
- Wu S B, Yu M H, Chen L. 2017. Nonmonotonic and spatial-temporal dynamic slope effects on soil erosion during rainfall-runoff processes. *Water Resources Research*, 53(2): 1369–1389.
- Wu S B, Chen L, Wang N L, et al. 2019. Two-dimensional rainfall-runoff and soil erosion model on an irregularly rilled hillslope. *Journal of Hydrology*, 580: 12346, doi: 10.1016/j.jhydrol.2019.12346.
- Xu X X, Ju T J, Zheng S Q. 2013. Sediment sources of Yan'gou watershed in the Loess Hilly region China under a certain rainstorm event. Springerplus, 2(Supp1): S2, doi: 10.1186/2193-1801-2-S1-S2.
- Zhao J L, Yang Z Q, Govers G. 2019. Soil and water conservation measures reduce soil and water losses in China but not down to background levels: evidence from erosion plot data. *Geoderma*, 337: 729–741.